Food & Function

ROYAL SOCIETY OF CHEMISTRY

PAPER

View Article Online
View Journal | View Issue

Cite this: *Food Funct.*, 2026, **17**, 4051

Therapeutic effects of selenium-enriched rapeseed against triple-negative breast cancer: involvement of Resolvin D5 activation and IL-17 signaling inhibition

Yuxin Lin,[a,d] Tangyi Wang,[b] Zhijing Wu,[b] Li Wang,[b] Zhiyao Yu,[b] Jiangyun Wang,[a] Tao Liu,[b] Xiaoling Cai,[b] Haoran Li,[b] Yanming Ren,[a] Zhanhai Su,[b,d] Shoude Zhang,[c,d] Juan An,[b,d] Qiong Wu*[b,d] and Haiyan Wang *[b,d]

Triple-negative breast cancer (TNBC) presents a major therapeutic challenge due to its aggressive behavior and a microenvironment characterized by a dysregulated axis linking inflammation to tumor progression. As a selenium-biofortified edible vegetable, selenium-enriched rapeseed shoots (SeRS) are a promising dietary source of methylselenocysteine (MSC), highlighting their potential in "medicine-food homology" strategies. This study aimed to investigate the chemo-preventive efficacy of selenium-enriched SeRS as a dietary intervention in TNBC, building upon its previously documented anti-inflammatory and antioxidant properties, and to elucidate its underlying mechanism of action. We first demonstrated that SeRS aqueous extract significantly inhibited the migration and invasion of 4T1 TNBC cells *in vitro*. Subsequently, in a preventive dietary intervention study, administration of SeRS potently suppressed orthotopic tumor growth and metastasis in a 4T1 syngeneic mouse model. Concomitantly, SeRS treatment favorably remodeled the tumor immune microenvironment, as evidenced by increased infiltration of $CD4^+$ and $CD8^+$ T cells and a decrease in exhausted $PD\text{-}1^+/LAG\text{-}3^+$ T cell subsets. Integrated metabolomic and transcriptomic analyses identified resolvin D5 (RvD5), a specialized pro-resolving mediator, as a key endogenous metabolite upregulated by SeRS, and revealed the pro-inflammatory IL-17 signaling pathway as a potential target. Molecular docking confirmed high-affinity binding between RvD5 and IL-17A. Functionally, both SeRS and purified RvD5 suppressed IL-17 pathway activation, as evidenced by reduced phospho-p65 and downregulation of IL-17 receptor (IL-17RA) and ACT-1. Critically, rescue experiments established that RvD5 could reverse IL-17A-induced pro-tumorigenic effects. Our findings elucidate a coordinated mechanism in which SeRS, *via* upregulation of RvD5, suppresses the IL-17 signaling pathway—a key driver of chronic inflammation and immune dysfunction in TNBC—thereby exerting anti-TNBC effects. This work provides a scientific basis for developing selenium-enriched agricultural products into functional foods for cancer prevention through targeted nutritional modulation.

Received 26th December 2025,
Accepted 2nd April 2026

DOI: 10.1039/d5fo05648a

rsc.li/food-function

1 Introduction

TNBC is defined as a particularly formidable clinical challenge, defined by the absence of targetable receptors. This notably contributes to its aggressive behavior, frequent recurrence, and a constrained spectrum of effective treatments. Conventional chemotherapies, while initially effective, often result in therapeutic resistance and disease relapse, underscoring the urgent need for novel, prevention-oriented strategies with favorable safety profiles.[1] In this context, functional foods-particularly those aligned with the traditional paradigm of the food-medicine continuum-hold exceptional promise. They offer the potential for synergistic bioactivity with reduced toxicity compared to single-agent pharmaceuticals, making them ideal candidates for long-term preventive interventions.[2] A compelling target for such strategies lies in the chronically inflamed tumor microenvironment, a hallmark of TNBC that sustains tumor progression, immune evasion, and therapeutic resistance.[3] Pro-inflammatory cytokines such as IL-17 and

[a]*Department of Traditional Chinese Medicine, Qinghai University Medical College, Xining, Qinghai, China*
[b]*Department of Basic Medical Sciences, Qinghai University Medical College, Xining, Qinghai, China*
[c]*State Key Laboratory of Plateau Ecology and Agriculture, Qinghai University, Xining, Qinghai, China*
[d]*Joint Research Center of Engineering Medicine for High-Altitude Cardio-Cerebrovascular Health, Xining, Qinghai, China*

TNF-α drive the activation of NF-κB and other downstream signaling cascades, creating a feed-forward loop that reinforces a tumor-promoting immune landscape.[4,5] Disrupting this chronic inflammatory circuitry therefore represents a rational, mechanism-based target for dietary intervention in TNBC.

SeRS, a member of the Brassicaceae (cruciferous) family cultivated through precision agricultural biofortification, emerge as a prime candidate to test this strategy. Unlike inorganic selenium compounds with a narrow therapeutic window, SeRS accumulates MSC as its primary selenium species—an organic selenium with a demonstrated enhanced safety profile and multi-faceted chemopreventive mechanisms.[6,7] Beyond selenium, the complete SeRS food matrix comprises a complex array of innate bioactive components, including glucosinolates and flavonoids, which are themselves known for direct free-radical scavenging and anti-inflammatory activities.[8]

We hypothesize that this holistic composition enables SeRS to exert superior, multi-targeted effects by actively resolving chronic inflammation and remodeling the immunosuppressive tumor microenvironment. To translate this hypothesis into an evidence-based dietary strategy, the present study was designed to evaluate the anti-TNBC efficacy of SeRS in preclinical models using physiologically relevant doses, to identify the key functional mediators mobilized by SeRS through an unbiased untargeted metabolomics approach, to elucidate the mechanistic axis by which SeRS modulates inflammatory signaling pathways within the tumor microenvironment, and to assess the immunomodulatory consequences of SeRS intervention-particularly its impact on T cell infiltration and exhaustion phenotypes. Collectively, this work aims to provide a mechanistic foundation for the application of selenium-enriched functional foods in TNBC prevention and adjuvant therapy, and to establish a discovery-driven paradigm for investigating complex food–host interactions within the "food-medicine continuum".

2 Materials and methods

2.1 Chemicals and reagents

Olaparib was obtained from Selleck. RvD5 (Catalog No. GC40982) was purchased from GLpBio. Recombinant mouse IL-17A protein (Catalog No. TMPY-02900) and recombinant human IL-17A protein (Catalog No. TMPY-02886) were acquired from Topscience. For *in vitro* studies, small-molecule compounds were dissolved in DMSO, while protein reagents were reconstituted according to the manufacturers' instructions.

2.2 Source and chemical characterization of the SeRS extract

SeRS aqueous extract used in the present study was prepared as described in section 2.1. The chemical composition of this extract has been comprehensively characterized in our prior collaborative work. High-performance liquid chromatography-inductively coupled plasma mass spectrometry (HPLC-ICP-MS) analysis confirmed that MSC was the predominant selenium species, accounting for the majority of selenium in the extract with a transfer ratio of 79.30% into the WE fraction.[9] Only trace amounts of other selenium forms were detected.

As reported therein, the water extract (WE) fraction, which corresponds directly to the aqueous extract used in this study, was found to contain a total selenium content of 140.56 μg g^{-1}.

2.3 Preparation of SeRS and CRS aqueous extract

Aqueous extracts of SeRS and conventional rapeseed shoots (CRS) were prepared using the following procedure. Briefly, the freeze-dried and finely powdered SeRS or CRS was suspended in ice-cold double-distilled water (ddH_2O) at a ratio of 1 : 10 (w/v). Using an ultrasonic cell disruptor (JY92-IIDN, LiChen, China) operated at 200 W for 5 minutes in an ice bath, with a duty cycle of 5 seconds on and 5 seconds off to prevent overheating. The resulting homogenate was centrifuged at 12 000*g* for 20 minutes at 4 °C. The supernatant was collected, sequentially filtered through 0.45 μm and 0.22 μm membrane filters, and lyophilized (SCIENTZ-20F/A, Scientz, China) to obtain a dry powder. To ensure consistency across batches, the extraction yield was calculated, and the final extract was standardized based on its dry weight. The resultant powder was kept at −80 °C until needed. Immediately before all assays, the extract was reconstituted in PBS or complete cell culture medium to the specified concentration. To confirm the reproducibility of the extraction process, three independent batches were prepared. All batches exhibited consistent anti-proliferative activity against 4T1 cells, with comparable half-maximal inhibitory concentration values.

2.4 Cell culture

The human TNBC cell line MDA-MB-231 and the mouse TNBC cell line 4T1 were obtained from Procell Life Science & Technology Co., Ltd (Wuhan, China). Cells were cryopreserved using the supplier's freezing medium (Procell, China) to create working stocks, and all experiments were performed with cells revived from these stocks. Cells were routinely cultured in a humidified incubator maintained at 37 °C with a 5% CO_2 atmosphere. MDA-MB-231 cells were grown in Dulbecco's Modified Eagle Medium (DMEM, high glucose), while 4T1 cells were grown in Roswell Park Memorial Institute (RPMI)-1640 medium. Both media were supplemented with 10% (v/v) heat-inactivated fetal bovine serum (FBS) and 1% (v/v) penicillin–streptomycin solution (containing 100 U mL^{-1} penicillin and 100 μg mL^{-1} streptomycin) to constitute the complete growth medium. Culture media were replaced every 1–2 days. Cells were monitored daily and subcultured when they reached 80–90% confluence using 0.25% trypsin-EDTA.

2.5 CCK-8 cell viability assay

Following a 24 h adhesion period after seeding (5×10^4 cells per well in 96-well plates), MDA-MB-231 or 4T1 cells were treated with graded concentrations of test compounds (SeRS, CRS extracts or RvD5) for 24 h. Cell viability was then determined by adding 10 μL of CCK-8 reagent (Elabscience, China) to each well, incubating for 1–2 h at 37 °C, and reading the

absorbance at 450 nm on a microplate reader, in accordance with the kit protocol.

2.6 Scratch wound healing assay

Following the creation of a linear scratch in confluent monolayers (MDA-MB-231 and 4T1 cells, 5×10^5 cells per well) using a sterile pipette tip and subsequent PBS wash, cells were treated with serum-free medium containing SeRS, CRS, or RvD5. Wound closure was then monitored: images taken at 0 h and 24 h under a phase-contrast microscope were analyzed in ImageJ to measure wound areas (A_0, A_{24}) and calculate the percentage closure as $(1 - A_{24}/A_0) \times 100\%$. All assays were conducted in triplicate and independently replicated three times.

2.7 Transwell migration and invasion assay

Cell migration and invasion capabilities were evaluated using Transwell chambers (Corning, USA). For the invasion assay, the upper chambers were pre-coated with 30 μL Matrigel Matrix (Corning, USA) and incubated at 37 °C for 1 hour to form a basement membrane matrix before cell seeding. Subsequent to a 20 h incubation under standard conditions (37 °C, 5% CO_2), cotton swabs were used to meticulously remove any cells that had not invaded from the top of the membrane. The invasive cells on the lower membrane surface then underwent fixation (4% paraformaldehyde, 15 min) and staining (0.1% crystal violet, 10 min) before being imaged with an inverted microscope. Employing ImageJ software, the degree of invasion was quantified by counting the stained cells present in five randomly chosen fields of view for each well.

2.8 Acute oral toxicity study in rats

The acute oral toxicity test for SeRS was performed as prescribed by OECD Guideline 425, employing Sprague-Dawley rats that weighed 180–220 g. After an acclimatization period, rats were fasted overnight and administered a single oral dose of SeRS aqueous extract at 2000 mg kg^{-1} (n = 5). The control group was defined by the administration of the vehicle (saline) at an equal volume. All animals were observed meticulously for the first 4 hours post-dosing, and then twice daily for 14 days for any signs of morbidity, mortality, or behavioral changes. Body weight and food consumption were recorded daily. At the study endpoint, all animals were humanely sacrificed. Blood was immediately collected for analysis, and key visceral organs (heart, liver, spleen, lungs, and kidneys) were excised and weighed, and subjected to gross necropsy and histopathological examination.

2.9 Animal model and drug administration

The study received the necessary ethical approval (Medical Research Ethics Committee, Qinghai University Medical College) prior to commencement. All subsequent animal experiments adhered to established guidelines and were performed in accordance with this obtained approval. Euthanasia was carried out by CO_2 inhalation (10–30%) overdose confirmed by cervical dislocation. All procedures adhered to protocols designed to minimize discomfort. An orthotopic model of TNBC was generated in female BALB/c mice. The mice, aged 4–5 weeks and weighing 16–20 g, were sourced from Henan Spike's Biological Technology Co., Ltd. After one week of acclimatization, mice for the first efficacy study were randomly assigned to groups (n = 8 per group). Mice in the Saline Control, SeRS, and CRS groups commenced preventive oral gavage for 14 consecutive days prior to tumor inoculation, receiving saline, SeRS aqueous extract (300 mg kg^{-1}), and CRS extract (300 mg kg^{-1}), respectively. Following this phase, all mice were anesthetized, A volume containing 5×10^5 viable 4T1 cells was surgically implanted into the right fourth mammary fat pad to generate the orthotopic tumors. Oral gavage in these three groups continued post-inoculation. For mechanistic validation, an additional group of mice received an identical tumor cell inoculation (mirroring the primary model). Once tumor volumes in both cohorts approached 100 mm^3, animals with consistently sized tumors were enrolled to begin the treatment regimen.

In the first study, the MSC group began daily oral gavage of methylselenocysteine 5 mg kg^{-1}, and the Olaparib group received intraperitoneal injection of olaparib (50 mg kg^{-1}) every three days. In the second study, mice were allocated into groups (n = 5 per group): the Saline Control group received intraperitoneal injections of saline; the IL-17A group received recombinant mouse IL-17A protein (100 ng per mouse) every two days; and the RvD5 group received RvD5 (10 ng per mouse) every two days, all *via* intraperitoneal injection. Tumor dimensions were monitored every 2–3 days with a digital caliper, and volumes were calculated from the formula (width^2 × length)/2. The therapeutic intervention in all groups was continued for 14 days post-randomization, which occurred when tumors reached approximately 100 mm^3.

2.10 Dose justification based on physiological relevance

The working concentrations of SeRS extract for *in vitro* assays were determined based on dose–response curves in MDA-MB-231 and 4T1 cell lines, which yielded IC_{50} values of 478.7 μg mL^{-1} and 406.2 μg mL^{-1}, respectively. Subsequent functional experiments (*e.g.*, migration, invasion assays) employed concentrations below the IC_{50} (typically in the range of 100–300 μg mL^{-1}) to ensure measurable bioactivity while minimizing cytotoxicity. These concentrations were selected to explore the pharmacological effects and mechanisms of SeRS. For the *in vivo* study, the dose of SeRS aqueous extract (300 mg per kg per day) was selected based on our preliminary efficacy studies. The dose-finding experiment is shown in SI Fig. S3.

To justify its physiological relevance, we converted this mouse dose to a Human Equivalent Dose (HED) using the body surface area normalization method (conversion factor of 12.3). The HED is approximately 24.4 mg per kg per day, equating to a daily intake of about 1.46 g of the lyophilized extract for a 60 kg adult. Based on the determined total selenium content in SeRS (140.56 μg g^{-1}),[9] this HED would provide approximately 205 μg of selenium per day, which falls well within the recommended safe and adequate dietary range (60–400 μg per day for adults). In terms of actual food con-

sumption, this selenium intake could be achieved by consuming roughly 15 grams of fresh selenium-enriched rapeseed shoots daily (assuming 90% moisture content), which is a practical and reasonable amount in a human diet.

The CRS aqueous extract was administered at the same doses as SeRS in both cellular and animal experiments. This design ensures that any observed biological differences between the SeRS and CRS groups can be attributed specifically to the selenium-biofortification status, rather than to differences in dosage or other phytochemical components present in the rapeseed matrix. As a selenium-deficient control, CRS provides the baseline for evaluating the unique contribution of selenium enrichment.

The dose of MSC at 5 mg per kg per day *via* oral gavage was selected to provide a selenium-equivalent exposure based on the active dose of the parent SeRS extract. Given the total selenium content in SeRS (140.56 μg g^{-1}), the daily selenium intake from 300 mg kg^{-1} SeRS is approximately 42.2 μg Se per kg. The MSC dose was calculated to deliver a comparable amount of bioavailable, organic-form selenium. This dose translates to a HED of approximately 0.4 mg kg^{-1}, resulting in a daily selenium intake that is well within the upper limit of the safe and adequate dietary range (60–400 μg per day for adults) and aligns with common supplemental doses.

The dose of Olaparib at 50 mg kg^{-1}, administered *via* intraperitoneal injection every three days, is a well-established and efficacious regimen in preclinical studies of triple-negative breast cancer, particularly in models relevant to DNA damage response. This dosing schedule is selected to validate the therapeutic sensitivity of our orthotopic model against a clinically relevant standard-of-care agent. It is important to note that this preclinical dosage regimen is mechanistically oriented and corresponds to the clinical oral dosage of 300 mg twice daily used in patients with BRCA-mutated breast cancer.

The dose of recombinant mouse IL-17A protein at 100 ng per mouse, administered *via* intraperitoneal injection every two days, was selected based on its established use in mechanistic studies to explore the pathophysiological role of IL-17A in shaping the tumor immune microenvironment. This dose is intended to induce a significant and sustained biological response for pathway validation, rather than to represent a direct therapeutic intervention. The chosen regimen effectively models enhanced IL-17A signaling within the study timeframe.

2.11 Sample collection and processing

Mice were anesthetized with 2.5% isoflurane at the endpoint for blood collection *via* the retro-orbital route into serum separation tubes. Samples were processed by allowing clotting (30 min, RT) followed by centrifugation (3000*g*, 15 min, 4 °C). The resulting serum fractions were maintained at −80 °C until metabolomic analysis.

Following immediate blood collection, the mice underwent euthanasia through cervical dislocation. The primary tumors were then surgically excised from the mammary fat pad. Each tumor was weighed, and its dimensions were measured with digital calipers for volume calculation (volume = (width^2 × length)/2). Each tumor was divided into three portions under sterile conditions: one portion was snap-frozen in liquid nitrogen for metabolomics and transcriptomics; another portion was fixed in 4% paraformaldehyde for 24–48 hours for histopathological examination; and the final portion was placed in ice-cold RPMI-1640 medium for immediate preparation of single-cell suspensions for flow cytometry analysis.

2.12 Flow cytometry

For immune profiling, the study was terminated on day 15 by euthanizing mice under 2.5% isoflurane anesthesia. Excised tumors were promptly processed into single-cell suspensions. The tissues were first mechanically dissociated and then subjected to enzymatic digestion. This digestion was performed in RPMI-1640 medium supplemented with 2 mg mL^{-1} collagenase IV and 0.1 mg mL^{-1} DNase I (both from Thermo Fisher Scientific) for 45 minutes at 37 °C. After filtration through 70-μm strainers and erythrocyte lysis, leukocytes were isolated by Percoll density gradient centrifugation. For T cell immunophenotyping, single-cell suspensions were stained with a cocktail of fluorescently-labeled antibodies against CD3e, CD4, and CD8 (all from Thermo Fisher Scientific; see SI Table S1 for details). To detect IL-17A$^+$ Th17 cells, cells were first stimulated for 5 hours with a PMA/ionomycin cocktail in the presence of protein transport inhibitors to induce cytokine production and block its secretion. Subsequently, cells were fixed, permeabilized, and stained intracellularly with an anti-IL-17A antibody.

Flow cytometric analysis was conducted on 5×10^5 cells per sample to characterize the antitumor immune response. Using FlowJo software, cells were first gated on FSC and SSC parameters to exclude debris and aggregates. Subsequent analysis involved detailed immunophenotyping across multiple fluorescence channels. A detailed schematic illustrating the sequential gating strategy is provided in SI Fig. S1.

2.13 Transcriptomic analysis

Total RNA was extracted from MDA-MB-231 cells treated under three conditions: negative control (NC), SeRS and CRS using Trizol reagent (Vazyme). RNA quality was verified using agarose gel electrophoresis and spectrophotometry. Library construction and RNA sequencing were performed by Shanghai OE Biotech Co., Ltd. Differential expression analysis was conducted comparing SeRS *vs*. NC, CRS *vs*. NC, and SeRS *vs*. CRS. The threshold for significance was set as an absolute $\log_2$ fold change ($|\log_2 FC|$) greater than 1 combined with an adjusted *p*-value of less than 0.05. These genes then underwent Kyoto Encyclopedia of Genes and Genomes (KEGG) and Gene Ontology (GO) enrichment analysis aimed at identifying the biological pathways and functions most affected by the observed expression changes.

2.14 Metabolomic profiling of serum and tumor tissues

Serum and tumor tissue samples from mice in all experimental groups were subjected to comprehensive metabolomic analysis using the Level One 500 global metabolomics platform (Shanghai OE Biotech Co., Ltd) to investigate the metabolic

alterations induced by SeRS intervention. For serum samples, proteins were precipitated with pre-chilled methanol followed by centrifugation. Tumor tissue samples were homogenized in ice-cold methanol : water (4 : 1, v/v) and subsequently centrifuged to deproteinize and clarify the extract. The resulting supernatants from both sample types were collected for analysis. The metabolic profiling was performed using the Level One 500 full-spectrum metabolomics approach. Prior to pattern recognition, raw data from both serum and tumor tissues To uncover differentially abundant metabolites, the raw metabolomic data from serum and tumor samples were initially processed through the XCMS platform (v4.5.1), which performed baseline filtering, peak detection, integration, and retention time correction. Following this, Principal component analysis (PCA) and Partial least squares discriminant analysis (PLS-DA) were then employed as multivariate statistical tools for pattern recognition and biomarker screening.

The following stringent criteria were applied to identify significantly altered metabolites: VIP > 1.0 from the PLS-DA model, |fold change| > 2.0, and a statistical p-value < 0.05. Metabolite identification was performed by matching exact mass and retention time with authentic standards in the HMDB database.

2.15 Network pharmacology analysis

Potential therapeutic targets for TNBC were retrieved from the GeneCards, OMIM, and DisGeNET databases using "triple-negative breast cancer" as the search term, Potential "disease targets" for TNBC were defined as those with scores surpassing the calculated median. The interaction network between RvD5 and TNBC-associated targets was constructed to explore potential mechanisms. Functional enrichment analysis was subsequently performed to identify significantly enriched pathways.

2.16 Molecular docking

For molecular docking, the 3D crystal structure of IL-17A was downloaded from the Protein Data Bank. The chemical structure file of RvD5 was obtained from the PubChem database. To predict the potential binding conformation between RvD5 and IL-17A, molecular docking was conducted utilizing the AutoDock Vina software. Protein and ligand preparation, including the addition of polar hydrogen atoms and charge calculation, was conducted prior to docking. The resulting docking poses were visualized and analyzed using the PyMOL molecular graphics system.

2.17 Western blot analysis

After treatment with SeRS, CRS, RvD5, or recombinant IL-17A protein for 24 hours, following protein extraction with inhibitor-supplemented RIPA buffer on ice and BCA quantification, equal protein aliquots (20 μg) underwent SDS-PAGE (10%) and transfer to PVDF membranes. Immunoblotting was then carried out by blocking (5% non-fat milk, 1 h, RT), incubating with primary antibodies overnight at 4 °C, washing with TBST, and incubating with HRP-conjugated secondaries (1 h, RT); signal detection employed an enhanced chemiluminescence system. Data derive from three independent replicates, with antibodies itemized in SI Table S2.

2.18 Statistical analysis

A p-value of less than 0.05 was considered statistically significant, with the following asterisk notation: $^{*}p < 0.05$, $^{**}p < 0.01$, $^{***}p < 0.001$, and $^{****}p < 0.0001$. Based on this criterion, data from at least three independent replicates ($n \geq 3$) are presented as mean ± standard deviation (SD). All statistical comparisons were conducted using GraphPad Prism software (version 9.0), employing an unpaired Student's t-test for comparisons between two groups or one-way analysis of variance (ANOVA) for comparisons among multiple groups.

3 Results

3.1 The anti-TNBC efficacy of SeRS from cellular to animal models

The anti-TNBC activity of SeRS was evaluated *in vitro*. Treatment with SeRS aqueous extract for 24 h dose-dependently inhibited viability in MDA-MB-231 and 4T1 cells, with IC_{50} values of 478.7 μg mL^{-1} and 406.2 μg mL^{-1}, respectively. CRS showed no cytotoxicity up to 1000 μg mL^{-1} (Fig. 1A–D). SeRS, but not CRS, significantly inhibited cell migration and invasion in wound healing and Transwell assays (Fig. 1E–H). In a syngeneic 4T1 mouse model, prophylactic oral administration of SeRS (300 mg kg^{-1}) suppressed tumor growth compared to saline and CRS controls, as shown by tumor volume, weight, and gross morphology (Fig. 1I–L). SeRS also synergized with olaparib in a therapeutic setting. An acute oral toxicity study in rats revealed no adverse effects (SI Fig. S2).

3.2 Transcriptomic analysis reveals SeRS-induced modulation of inflammatory and immune networks in TNBC cells

RNA sequencing of MDA-MB-231 cells showed clear segregation among SeRS, CRS, and control groups by principal component analysis (Fig. 2A). Differential expression analysis identified genes uniquely modulated by SeRS relative to both control and CRS (Fig. 2B–E). GO enrichment analysis indicated significant altera (Fig. 2F). KEGG pathway analysis revealed that SeRS modulated pathways related to cancer progression, cholesterol metabolism, unsaturated fatty acid biosynthesis, and the IL-17 signaling pathway (Fig. 2H). Comparative analysis of SeRS *vs.* CRS showed specific enrichment of inflammatory response and cytokine-mediated signaling (Fig. 2G). KEGG enrichment further demonstrated stronger modulation of TNF, NF-κB, IL-17, and Toll-like receptor signaling by SeRS than by CRS (Fig. 2I).

3.3 SeRS alleviates systemic inflammation and reverses T-cell exhaustion in the tumor microenvironment

SeRS treatment significantly reduced serum levels of TNF-α, IL-6, and IL-17A (Fig. 3A–C). Flow cytometry revealed increased intratumoral infiltration of $CD4^{+}$ and $CD8^{+}$ T cells in SeRS-treated mice (Fig. 3D–F). Compared to controls, SeRS

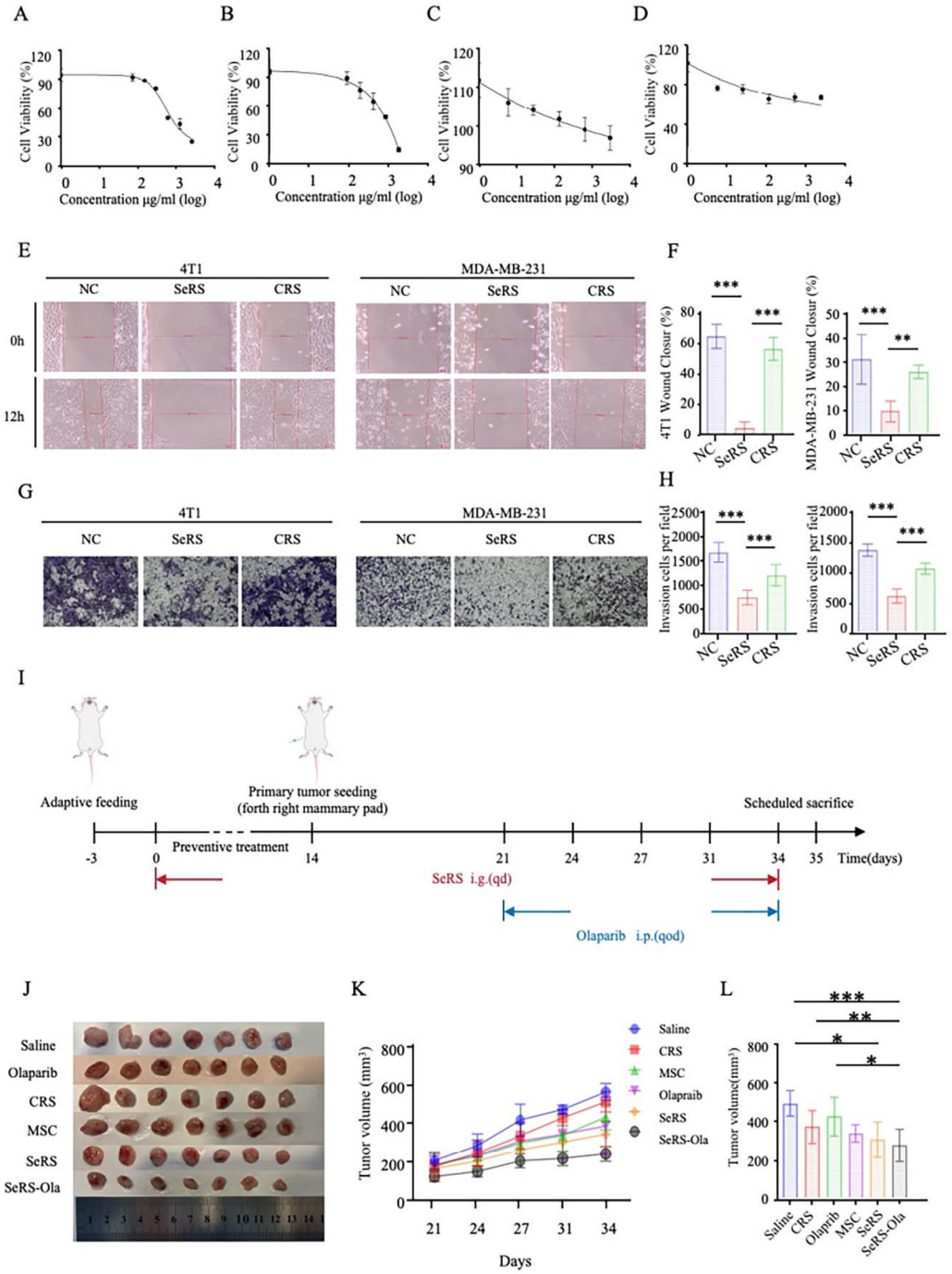

Fig. 1 Antitumor activity of SeRS and CRS *in vitro* and *in vivo*. (A–D) Dose–response curves of SeRS and CRS in breast cancer cells. The half-maximal IC_{50} of (A) SeRS on 4T1 cells, (B) SeRS on MDA-MB-231 cells, (C) CRS on 4T1 cells, and (D) CRS in MDA-MB-231 cells are shown. Data are presented as the mean ± SEM of three independent experiments. (E and F) Wound healing assay assessing cell migration. (E) Representative microscopic images of scratch wounds in 4T1 and MDA-MB-231 cell monolayers at 0 h and 24 h after treatment with NC, SeRS, or CRS. Scale bar = 100 μm. (F) Data for the relative wound healing rate are shown as mean ± SEM (n = 3). Statistical comparisons were made using one-way ANOVA, with significance denoted as [*p < 0.05, **p < 0.01, ***p < 0.001 compared to the NC group]. (G and H) Transwell invasion assay. (G) Representative images of 4T1 and MDA-MB-231 cell invasion after 24 h exposure to NC, SeRS, or CRS (scale bar = 100 μm). (H) Quantification of invaded cells. Data are presented as mean ± SEM (n = 3). Differences were analyzed using one-way ANOVA [*p < 0.05, **p < 0.01, ***p < 0.001 compared to NC]. (I) Schematic of the prophylactic animal study design. The timeline illustrates the administration of SeRS or CRS prior to and following the inoculation of 4T1 cells into the mammary fat pads of mice. (J) Representative photographs of excised tumors from each group at the study endpoint. (K) Tumor growth curves. Tumor volumes in 4T1 tumor-bearing mice from the NC, SeRS, and CRS treatment groups were measured every two days. Tumor volume was calculated as (length × width^2)/2. (L) Final tumor volumes. Comparison of tumor sizes at the study endpoint. Values are shown as mean ± SEM. Significance was determined *via* one-way ANOVA [*p < 0.05, **p < 0.01, ***p < 0.001].

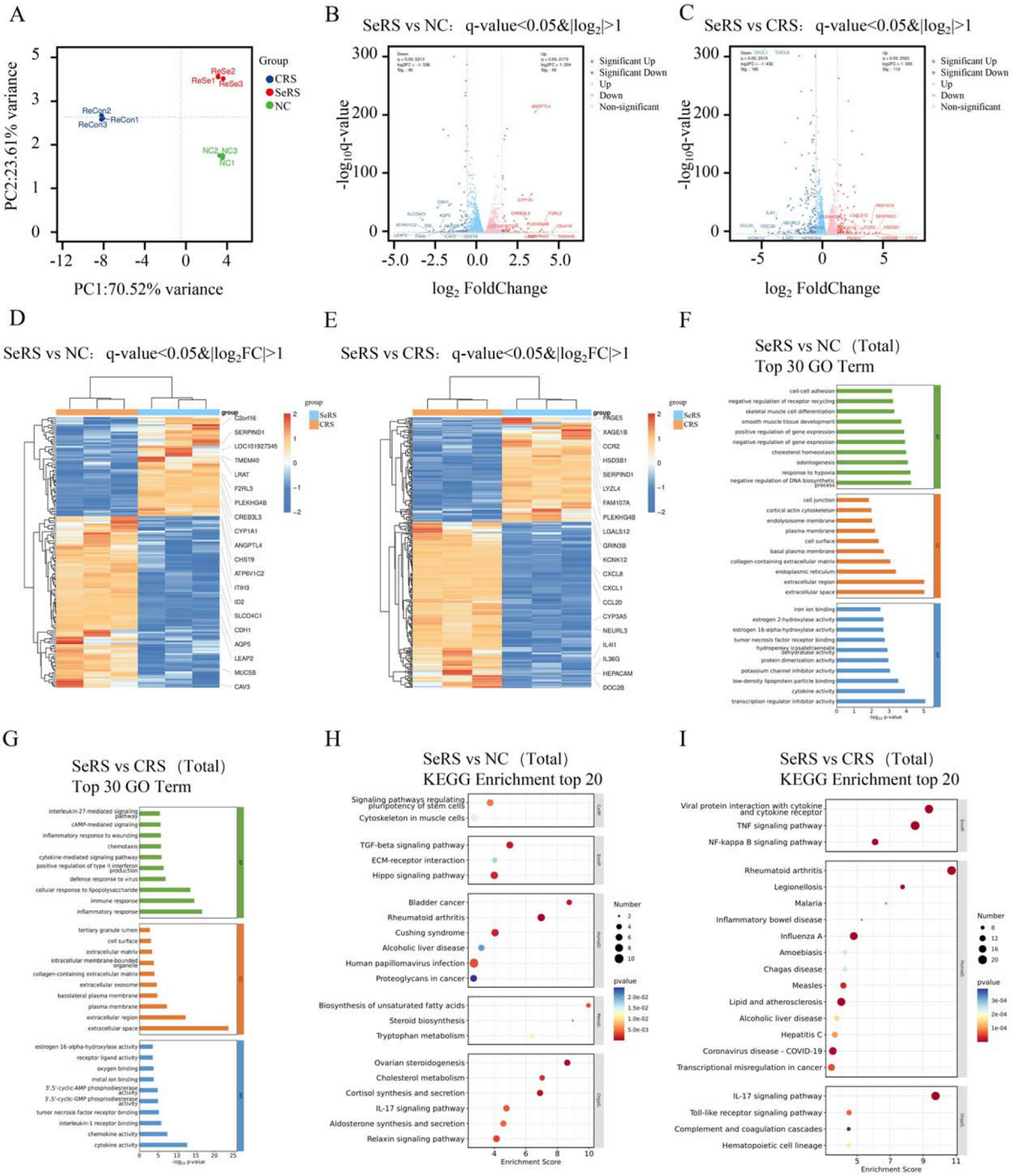

Fig. 2 Transcriptomic profiling of MDA-MB-231 cells treated with SeRS and CRS. (A) PCA plot illustrates the global showing global transcriptomic variation across samples from the NC, SeRS-treated, and CRS-treated groups. (B and C) Volcano plots of differentially expressed genes (DEGs) in the (B) SeRS *vs.* NC and (C) SeRS *vs.* CRS comparisons. Genes with $|\log_2(\text{fold change})| > 1$ and adjusted p-value (q) < 0.05 are highlighted in red (up-regulated) or blue (down-regulated). (D and E) Heatmaps of differentially expressed genes. Hierarchical clustering of DEGs (D) between SeRS and NC groups, and (E) between SeRS and CRS groups. Only genes meeting the criteria of $|\log_2 FC| > 1$ and q-value < 0.05 are displayed. (F and G) GO enrichment analysis. The bar charts display the top 30 enriched GO terms (Biological Process) for the total set of DEGs (F) in the SeRS *vs.* NC comparison and (G) in the SeRS *vs.* CRS comparison. Terms are ranked by $-\log_{10}(q\text{-value})$. (H–I) KEGG pathway enrichment analysis. The bar charts show the top 20 enriched KEGG pathways for the total set of DEGs (H) in the SeRS *vs.* NC comparison and (I) in the SeRS *vs.* CRS comparison. Pathways are ranked by $-\log_{10}(q\text{-value})$.

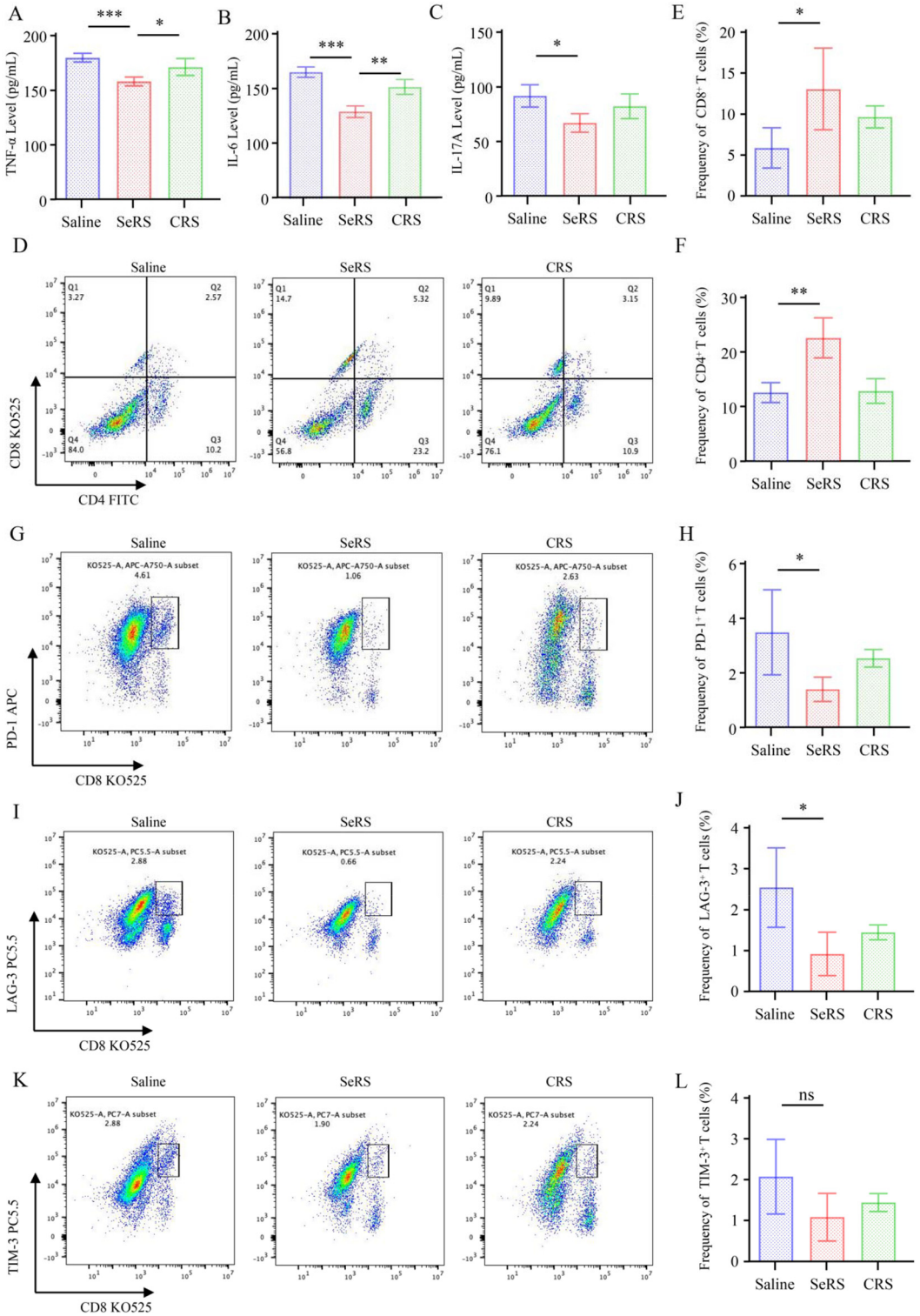

Fig. 3 SeRS modulates systemic inflammation and reinvigorates tumor-infiltrating T cells. (A–C) Serum levels of pro-inflammatory cytokines (A) TNF-α, (B) IL-6, and (C) IL-17A at the experimental endpoint, as determined by ELISA. Data are expressed as pg mL^{-1} (mean ± SEM, n = 5). (D) Representative flow cytometry plots of tumor-infiltrating $CD4^+$ and $CD8^+$ T cells. Gating strategy for identifying $CD3^+CD4^+$ and $CD3^+CD8^+$ T cell subsets. (E and F) Quantification of major T cell subsets. Proportions of (E) $CD8^+$ T cells and (F) $CD4^+$ T cells among tumor-infiltrating lymphocytes. (G, I and K) Representative flow cytometry plots of T cell exhaustion markers. Expression profiles of (G) PD-1, (I) LAG-3, and (K) TIM-3 on tumor-infiltrating $CD8^+$ T cells from different treatment groups. (H, J and L) Frequencies of $CD8^+$ T cells expressing (H) PD-1, (J) LAG-3, and (L) TIM-3. Data are presented as mean ± SEM (n = 5). Statistical significance was determined by one-way ANOVA followed by Tukey's *post hoc* test. *p < 0.05, **p < 0.01, ***p < 0.001.

decreased the frequency of PD-1$^+$/LAG-3$^+$ CD8$^+$ T cells, while TIM-3$^+$ frequency remained unchanged (Fig. 3G–L).

3.4 Integrated multi-omics identifies RvD5 as a key mediator linking SeRS to IL-17 pathway suppression

Our metabolomic profiling revealed a distinct reprogramming of the lipid mediator landscape. Analysis of differential metabolites *via* UpSet plot demonstrated that RvD5 consistently emerged as a shared, upregulated metabolite across multiple comparison groups (Fig. 4A–E). To transcend a mere list of alterations and understand functional interactions, we constructed a global correlation network. Within this network, RvD5 was identified as a highly connected hub node (indegree ≥ 2). The identification of RvD5 was further validated by secondary mass spectrometry in both serum and tumor tissue datasets. The characteristic fragmentation patterns, with a primary ion at m/z 359.2225, confirmed its structural identity with excellent matching to reference spectra (Fig. 4F–H). To functionally interrogate RvD5's role, we performed a network pharmacology analysis predicting its targets against TNBC. GO enrichment analysis revealed significant involvement in inflammatory response regulation and immune cell activation (Fig. 4J). A significant enrichment of predicted RvD5 targets within the IL-17 signaling pathway was identified through KEGG analysis (Fig. 4I). This computational prediction aligns with our independent transcriptomic profiles from MDA-MB-231 cells, where the IL-17 pathway was significantly downregulated in both the SeRS *vs.* NC and SeRS *vs.* CRS comparisons. This convergence of evidence from orthogonal approaches strongly implicates the IL-17 pathway as a pivotal and specific target of SeRS action, likely mediated by RvD5. To explore the physical basis of this targeting, molecular docking was performed between RvD5 and IL-17A. The simulation revealed a robust binding affinity with a docking score of -6.043 kcal mol^{-1} (Fig. 4K).

3.5 RvD5 suppresses TNBC cell proliferation, migration, and invasion *via* inhibiting the IL-17 pathway

The functional impact of RvD5 on TNBC was evaluated by examining its influence on key cellular behaviors—viability, migration, and invasion—in 4T1 and MDA-MB-231 cell lines. A CCK-8 assay revealed that RvD5 treatment for 24 hours dose-dependently inhibited cell proliferation, with half-maximal IC_{50} values of 24.92 nM in 4T1 cells and 77.42 nM in MDA-MB-231 cells (Fig. 5A). Consistent with its anti-proliferative activity, RvD5 significantly impeded cell migration, as evidenced by delayed scratch wound closure in both cell lines after 24 hours (Fig. 5B). Furthermore, Transwell invasion assays demonstrated that RvD5 potently suppressed the invasive capacity of TNBC cells (Fig. 5C). Western blot showed that SeRS and RvD5, but not CRS, downregulated IL-17RA, ACT-1, and p-p65, with total p65 unchanged (Fig. 5D and E).

3.6 RvD5 mediates the anti-TNBC effects of SeRS by suppressing the IL-17 signaling pathway

We treated MDA-MB-231 and 4T1 cells with recombinant IL-17A protein to activate the pathway. Subsequent western blot analysis confirmed that IL-17A stimulation significantly upregulated the expression of IL-17RA and its adaptor protein ACT-1, and increased the phosphorylation of the key downstream effector p65 (Fig. 6A).

Strikingly, the co-administration of either SeRS aqueous extract or purified RvD5 substantially attenuated these IL-17A-induced molecular changes. In both cell lines, the "IL-17A + SeRS" and "IL-17A + RvD5" treatment groups showed a marked downregulation of IL-17RA and ACT-1 protein levels, along with a significant reduction in p-p65 (Fig. 6A). Densitometric quantification of the blots confirmed that both SeRS and RvD5 effectively reversed the activation of the IL-17 signaling cascade induced by IL-17A stimulation in 4T1 and MDA-MB-231 cells (Fig. 6B and C).

3.7 RvD5 antagonizes IL-17A-driven tumor progression and Th17 polarization *in vivo*

To validate the functional relevance of the SeRS-RvD5-IL-17 axis in a physiological setting, we conducted an *in vivo* intervention study (Fig. 6D). Mice bearing orthotopic 4T1 tumors were treated with Saline, RvD5 alone, recombinant IL-17A protein alone, or a combination of IL-17A and RvD5.

Consistent with its tumor-promoting role, IL-17A administration significantly accelerated tumor growth compared to the Saline control, as shown by longitudinal volume tracking and representative tumor images (Fig. 6E and F). Strikingly, this pro-tumorigenic effect was effectively counteracted by the co-administration of RvD5 (Fig. 6E and F). Quantitative analysis of the final tumor volumes confirmed that RvD5 alone reduced tumor burden, and more importantly, it abrogated the tumor-promoting effect of IL-17A (Fig. 6G).

Flow cytometric analysis of splenocytes revealed that IL-17A treatment induced a significant expansion of pro-tumorigenic Th17 cells (CD4$^+$ IL-17A$^+$ T cells). Notably, this IL-17A-driven Th17 polarization was markedly reversed by concurrent RvD5 treatment (Fig. 6H and I).

4. Discussion

TNBC remains a high-risk subtype with limited targeted options, prompting increasing interest in safe, dietary strategies that intercept core pathological drivers such as chronic inflammation and oxidative stress.[10,11] This study provides compelling evidence that SeRS a selenium-biofortified cruciferous vegetable, exert significant anti-TNBC effects through a coordinated mechanism involving the mobilization of RvD5 and suppression of the IL-17 signaling pathway. Our findings bridge the concept of the "food-medicine continuum" with metabolic-immune crosstalk, highlighting a dietary strategy for TNBC suppression in preclinical models.

4.1. The SeRS-RvD5-IL-17 axis: an integrated mechanistic framework

Our integrated multi-omics and functional analyses reveal a cohesive axis wherein whole-food SeRS matrix exerts its anti-TNBC effects. We demonstrate that SeRS treatment uniquely

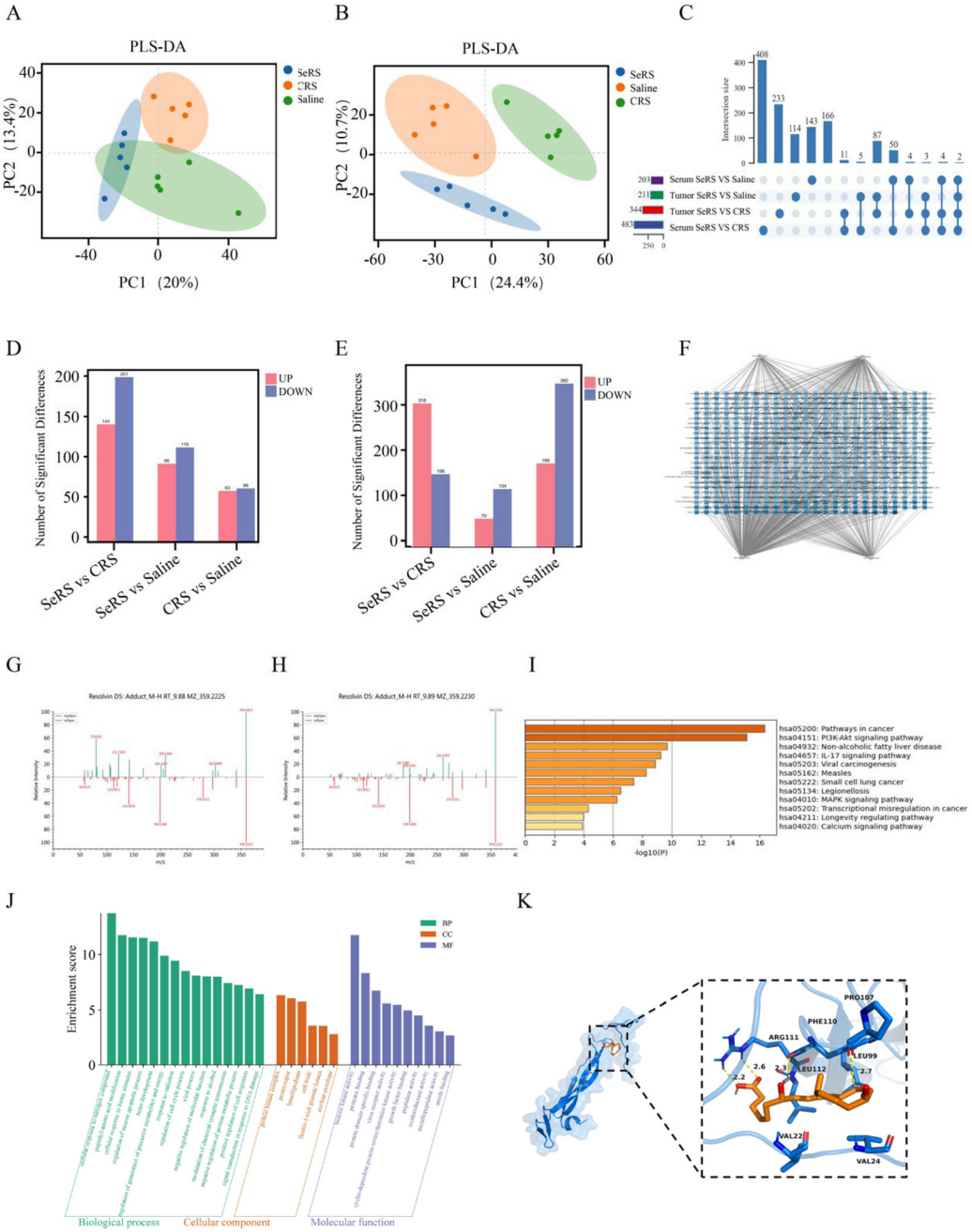

Fig. 4 Metabolic reprogramming induced by SeRS and identification of the key metabolite RvD5. (A and B) PLS-DA score plots derived from metabolomic profiles of (A) tumor tissues and (B) serum, showing separation among the Saline, CRS, and SeRS treatment groups. Each point represents an individual sample. (C) Intersection of differentially abundant metabolites (DAMs). An UpSet plot illustrating the overlaps among the sets of DAMs identified in four comparisons: SeRS *vs.* Saline and SeRS *vs.* CRS in both tumor tissue and serum. (D and E) Quantitative summary of DAMs. Bar charts showing the number of up- and down-regulated metabolites in (D) tumor tissue and (E) serum based on the SeRS *vs.* saline comparison. (F) Correlation network of consensus DAMs. A network diagram depicting the correlations among the core set of DAMs commonly altered across the four comparisons detailed in (C). (G and H) MS/MS spectrum for metabolite identification. Fragmentation spectrum (MS^2) of RvD5 detected in (G) tumor tissue and (H) serum samples. The characteristic ion at *m/z* 359.2225 is indicated. (I and J) Network pharmacology prediction for RvD5 in TNBC. (I) KEGG pathway enrichment analysis and (J) GO enrichment analysis (including Biological Process-BP, Cellular Component-CC, and Molecular Function-MF terms) of potential targets linking RvD5 to TNBC. (K) Molecular docking visualization.3D representation of the predicted binding conformation between RvD5 and the IL-17A protein, highlighting key interaction sites. Data presentation & statistical analysis: metabolomics data are presented as mean values or relative abundances. Statistical thresholds for differential analysis (*p*-value, $|\log_2 FC|$, VIP) are specified in the respective figure panel descriptions.

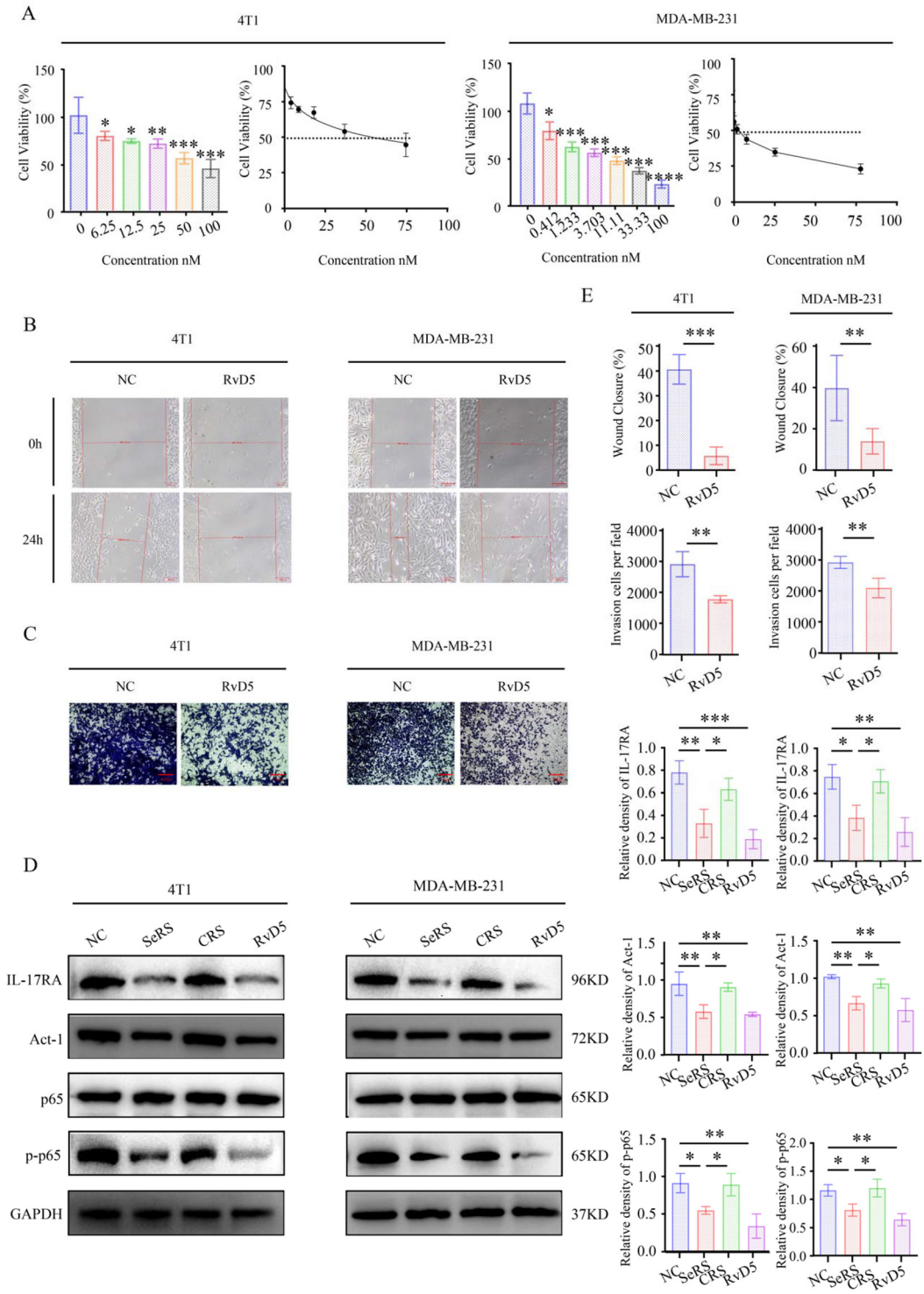

Fig. 5 *In vitro* antitumor effect of RvD5 and its impact on the IL-17A signaling pathway. (A) Cell viability assay. CCK-8 assay measuring the viability of 4T1 and MDA-MB-231 cells after 24 h exposure to RvD5. Data are expressed as mean ± SEM (n = 3). Significance *vs.* NC group was determined by unpaired Student's t-test (*p < 0.05, **p < 0.01, ***p < 0.001, ****p < 0.0001). (B) Wound healing assay. Representative microscopic images of scratch wounds in 4T1 (left panel) and MDA-MB-231 (right panel) cell monolayers at 0 h and 24 h after treatment with RvD5 or NC. Scale bar = 100 μm. (C) Transwell invasion assay. The images depict 4T1 (left panel) and MDA-MB-231(right panel) cells that invaded following a 24-hour treatment with RvD5 or NC (scale bar = 100 μm). (D) Western blot analysis showing protein levels of IL-17RA and ACT-1, and p-p65 in cells treated with SeRS, CRS, or RvD5. β-Actin served as a loading control. Significant differences *versus* the NC group are indicated (*p < 0.05, **p < 0.01, ***p < 0.001). (E) Quantitative summary. Graphical representation of the quantified data from the functional and protein expression assays. Significance levels are denoted as *p < 0.05, **p < 0.01, ***p < 0.001.

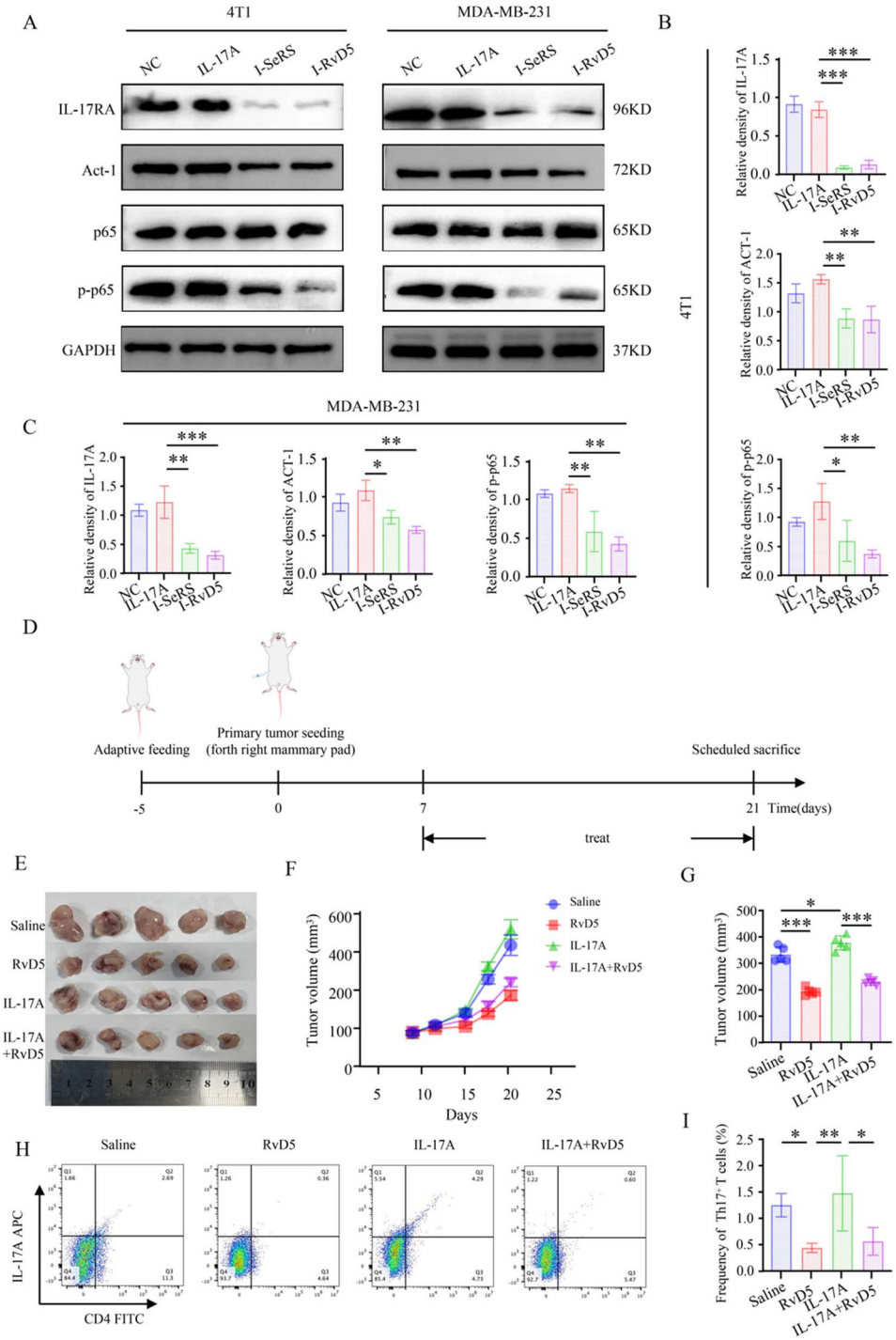

Fig. 6 Mechanism of RvD5 in mediating the anti-TNBC effects of SeRS *via* suppression of the IL-17 signaling pathway. (A–C) Western blot analysis of the IL-17A signaling pathway in 4T1 cells and MDA-MB-231cells. Protein levels of IL-17RA and ACT-1, and p-p65 in cells treated with: (A) recombinant IL-17A, (B) IL-17A combined with SeRS, and (C) IL-17A combined with RvD5. β-Actin served as a loading control.*$p < 0.05$, **$p < 0.01$, ***$p < 0.001$ *vs.* NC. (D) Schematic of the therapeutic animal experiment timeline. The diagram illustrates the treatment schedule following tumor inoculation and administration of SeRS, RvD5, and relevant modulators. (E) Representative photographs of excised tumors from each group at the study endpoint. (F) Tumor growth curves. Tumor volumes were measured every five days. Volume was calculated as (length × width^2)/2. (G) Final tumor volumes. Comparison of tumor sizes at the study endpoint. Values represent the mean ± SEM. Differences between groups were analyzed using one-way ANOVA. Statistical significance is indicated by asterisks: *$p < 0.05$, **$p < 0.01$, and ***$p < 0.001$. (H) Representative flow cytometry plots of splenic Th17 cells. Gating strategy for identifying Th17 cells (CD4$^+$IL-17A$^+$) in mouse spleen. (I) Quantification of splenic Th17 cells. Proportion of Th17 cells among splenic CD4$^+$ T cells across different treatment groups. Data presentation & statistical analysis: data are presented as mean ± SEM ($n = 5$), and group differences were evaluated by one-way ANOVA with *post-hoc* tests.

upregulates the specialized pro-resolving mediator (SPM) RvD5, which we identify as a key functional metabolite. Both SeRS and purified RvD5 potently inhibited the IL-17 signaling pathway *in vitro*, manifested as reduced p-p65 alongside the downregulation of key pathway components, including the receptor IL-17RA and the signaling adaptor ACT-1.[12,13] *In vivo*, RvD5 alone was sufficient to counteract the tumor-promoting and Th17-polarizing effects of exogenous IL-17A. These data position RvD5 as a functionally important downstream mediator of SeRS action, acting at least in part through antagonism of the pro-tumorigenic IL-17 pathway.

4.2. IL-17 suppression as a central driver of SeRS-mediated immune microenvironment remodeling

The IL-17 signaling pathway, identified by our transcriptomic analysis as a downregulated pathway following SeRS intervention, plays a well-documented pathogenic role in triple-negative breast cancer. IL-17 promotes tumor progression through multiple convergent mechanisms: it directly enhances cancer cell proliferation and invasiveness, recruits myeloid-derived suppressor cells, fosters an immunosuppressive microenvironment, and sustains chronic inflammation.[14,15] The functional consequence of this pathway inhibition is a profound and favorable reshaping of the tumor microenvironment. SeRS treatment significantly increased tumor-infiltrating $CD4^+$ and $CD8^+$ T cells, reduced circulating levels of pro-inflammatory cytokines (IL-6, IL-17A, TNF-α), and—most strikingly—selectively reversed the $PD\text{-}1^+/LAG\text{-}3^+$ exhaustion phenotype in $CD8^+$ T cells. These immune remodeling effects are temporally and contextually associated with the suppression of IL-17 signaling, and are consistent with the well-documented downstream consequences of IL-17 inhibition, including attenuation of oxidative stress, reduced neutrophil recruitment, and restoration of T-cell cytotoxicity[16,17] and are consistent with our observed phenotypes (increased $CD4^+/CD8^+$ T cell infiltration, reduced $PD\text{-}1^+/LAG\text{-}3^+$ exhausted subsets), although direct measurement of these downstream effectors in the current model was beyond the scope of this study and remains an open direction for future investigation.

Importantly, we acknowledge the boundaries of our evidence. While a substantial body of literature establishes that oxidative stress is a direct driver of T-cell exhaustion and that alleviation of oxidative stress restores T-cell function,[18–20] the present study did not directly measure oxidative stress markers in the tumor microenvironment. We therefore interpret the reduced frequencies of exhausted T cells as a likely downstream consequence of IL-17 pathway inhibition, but which awaits formal causal validation through perturbation experiments.

4.3. RvD5: a precious endogenous mediator bridging functional food and systemic resolution

Beyond its identified functional role, the unique biological attributes of RvD5 warrant further emphasis, as they underscore the sophistication of the mechanism elicited by SeRS. First, RvD5 is a precious endogenous mediator.[21] Unlike conventional nutrients or antioxidants that can be abundantly supplemented through diet, RvD5 itself is a potent, structurally-SPM[22] that is not present in significant quantities in foods. Its scarcity and instability make direct pharmacological administration challenging, elevating the strategy of stimulating its endogenous production as a particularly elegant therapeutic approach.[23] Second, its endogenous nature is key. RvD5 is enzymatically derived from dietary docosahexaenoic acid (DHA),[24] meaning that the body utilizes a nutrient to produce a highly targeted bioactive "resolution signal". Our finding that SeRS elevates RvD5 levels exemplifies a core principle of the "food-medicine continuum": a functional food does not merely deliver a drug-like compound, but rather primes and optimizes the body's inherent biochemical pathways to generate protective mediators. Third, RvD5's action transcends simple anti-inflammatory activity. As an SPM, it is part of an active resolution program that not only dampens inflammation[25] but also promotes the clearance of cellular debris and facilitates tissue homeostasis, representing a more advanced physiological response than mere suppression.[21] The high-affinity binding of RvD5 to IL-17A, as supported by our molecular docking, suggests it can act as a precise molecular brake on this pivotal pro-inflammatory and pro-oxidant pathway. Therefore, the upregulation of RvD5 by SeRS represents a pivotal link: the selenium-enriched food matrix empowers the host to mobilize a precious,[26] endogenous, and pro-resolving lipid mediator, which in turn orchestrates the suppression of the IL-17 axis and the subsequent alleviation of inflammation. This positions RvD5 not just as a biomarker, but as the central biological currency through which dietary intervention translates into a coordinated systemic protective response.

4.4. The holistic value of the functional food matrix

While MSC is a key bioactive component, our study highlights the superior efficacy of the whole SeRS food matrix over CRS. The broad, coordinated effects observed—from specific immunometabolic modulation to systemic immune reprogramming—likely arise from synergies between selenium compounds and other innate phytochemicals in rapeseed.[9] This supports the "food-medicine continuum" paradigm,[27] where a whole food offers multi-targeted, systems-level benefits that are difficult to replicate with single compounds, emphasizing its value for long-term preventive nutrition.

4.5. Limitations and future perspectives

Limitations of this study should be acknowledged. First, the primary mechanistic findings were obtained from murine models and await validation in human systems. Second, the precise upstream events linking SeRS intake to RvD5 elevation remain incompletely defined; the responsible selenium species, phytochemicals, and potential synergistic interactions within the SeRS matrix require systematic dissection. Third, although we have previously demonstrated SeRS-mediated enhancement of glutathione-dependent antioxidant capacity in other models, these redox parameters were not measured in the current TNBC study. Fourth, the causal relationship between IL-17 suppression, oxidative stress alleviation, and

reduced T-cell exhaustion has not been formally established through perturbation experiments; our interpretation remains hypothesis-driven and requires genetic or pharmacological validation. Fifth, the putative direct effect of RvD5 on T-cell exhaustion markers remains entirely speculative. These limitations do not diminish the core contribution of this work—the identification of a novel, nutritionally accessible SeRS-RvD5-IL-17 axis—but rather define clear boundaries and future directions for continued investigation.

5. Conclusion

In conclusion, this study identifies a previously unrecognized mechanism whereby dietary SeRS combats TNBC by mobilizing the endogenous pro-resolving mediator RvD5, which functions as a key effector by suppressing the pro-tumorigenic IL-17 pathway. This SeRS-RvD5-IL-17 axis is associated with remodeling of the immunosuppressive tumor microenvironment, enhanced $CD4^+$ and $CD8^+$ T cell infiltration, and reversal of $CD8^+$ T cell exhaustion. Notably, the effective dose exhibits a wide safety window and synergizes with anti-PD-1 therapy, highlighting its translational potential as a food-grade immunomodulatory adjuvant. Our findings provide a mechanistic foundation for developing SeRS-based functional foods and position the SeRS-RvD5-IL-17 axis at the interface of nutritional science and cancer immunology.

Author contributions

Conceptualization, H. W., Q. W. and J. A.; methodology, Y. L., T. W., Z. W. and T. L.; software, T. L. and H. L.; validation, Y. L., T. W., Z. W., L. W. and Z. Y.; formal analysis, Y. L., T. W. and Z. W.; investigation, Y. L., T. W., Z. W., L. W., Z. Y. and X. C.; resources, Z. S., S. Z., J. A., Q. W. and H. W.; data curation, Y. L., T. W. and Z. W.; writing—original draft preparation, Y. L. and T. W.; writing—review and editing, Z. S., J. A., Q. W., H. W., J. W., Y. R., X. C. and all other authors; visualization, Y. L., T. W. and Z. W.; supervision, Z. S., J. A., Q. W. and H. W.; project administration, Q. W. and H. W.; funding acquisition, Z. S., S. Z., J. A., Q. W. and H. W. All authors have read and agreed to the published version of the manuscript.

Conflicts of interest

The authors declare no conflicts of interest. The funders had no role in the design of the study; in the collection, analyses, or interpretation of data; in the writing of the manuscript; or in the decision to publish the results.

Data availability

The data supporting this article have been included in the article and its supplementary information (SI). Supplementary information is available. See DOI: https://doi.org/10.1039/d5fo05648a.

The data reported in this paper have been deposited in the OMIX, China National Center for Bioinformation/Beijing Institute of Genomics, Chinese Academy of Sciences (https://ngdc.cncb.ac.cn/omix: accession no. OMIX015206/15199).

Acknowledgements

The authors extend their sincere gratitude to Academician Hanzhong Wang and Professor Xiaoling Dun, along with their team at the Oil Crops Research Institute of the Chinese Academy of Agricultural Sciences, for their generous provision of the SeRS material, which was crucial to this study.

References

1 Y. Li, H. Zhang, Y. Merkher, L. Chen, N. Liu, S. Leonov and Y. Chen, Recent advances in therapeutic strategies for triple-negative breast cancer, *J. Hematol. Oncol.*, 2022, **15**, 121.
2 X. Xi, S. Hu, X. Zhang, P. An, Y. Luo, J. Luo and Y. Zhu, Bioactives in Food-As-Medicine for Special Medical Purposes, *Adv. Nutr.*, 2025, **16**, 100546.
3 N. M. Iyengar, A. Gucalp, A. J. Dannenberg and C. A. Hudis, Obesity and Cancer Mechanisms: Tumor Microenvironment and Inflammation, *J. Clin. Oncol.*, 2016, **34**, 4270–4276.
4 M. J. McGeachy, D. J. Cua and S. L. Gaffen, The IL-17 Family of Cytokines in Health and Disease, *Immunity*, 2019, **50**, 892–906.
5 M. J. Morgan and Z.-g. Liu, Crosstalk of reactive oxygen species and NF-κB signaling, *Cell Res.*, 2010, **21**, 103–115.
6 J. Ma, J. Huang, J. Sun, Y. Zhou, X. Ji, D. Guo, C. Liu, J. Li, J. Zhang and H. Song, L-Se-methylselenocysteine sensitizes lung carcinoma to chemotherapy, *Cell Prolif.*, 2021, **54**, e13038.
7 A. Bhattacharya, Methylselenocysteine: a promising antiangiogenic agent for overcoming drug delivery barriers in solid malignancies for therapeutic synergy with anticancer drugs, *Expert Opin. Drug Delivery*, 2011, **8**, 749–763.
8 S. Maina, G. Misinzo, G. Bakari and H.-Y. Kim, Human, Animal and Plant Health Benefits of Glucosinolates and Strategies for Enhanced Bioactivity: A Systematic Review, *Molecules*, 2020, **25**, 3682.
9 J.-P. Zhan, M. Qi, C. Wang, X.-F. Wang, H.-Z. Wang and X.-L. Dun, Precise Determination of Selenium Forms and Contents in Selenium-Enriched Rapeseed Seedlings and Flowering Stalks by HPLC-ICP-MS, *J. Agric. Food Chem.*, 2024, **72**, 9477–9486.
10 P. Zagami and L. A. Carey, Triple negative breast cancer: Pitfalls and progress, *NPJ Breast Cancer*, 2022, **8**, 95.
11 O. Obidiro, G. Battogtokh and E. O. Akala, Triple Negative Breast Cancer Treatment Options and Limitations: Future Outlook, *Pharmaceutics*, 2023, **15**, 1796.

12 N. I. Lorè, A. Bragonzi and C. Cigana, The IL-17A/IL-17RA axis in pulmonary defence and immunopathology, *Cytokine Growth Factor Rev.*, 2016, **30**, 19–27.
13 C. Ren, X. Han, C. Lu, T. Yang, P. Qiao, Y. Sun and Z. Yu, Ubiquitination of NF-κB p65 by FBXW2 suppresses breast cancer stemness, tumorigenesis, and paclitaxel resistance, *Cell Death Differ.*, 2021, **29**, 381–392.
14 H. Liao, X. Chang, L. Gao, C. Ye, Y. Qiao, L. Xie, J. Lin, S. Cai and H. Dong, IL-17A promotes tumorigenesis and upregulates PD-L1 expression in non-small cell lung cancer, *J. Transl. Med.*, 2023, **21**, 828.
15 L. Wu, Y. Jin, X. Zhao, K. Tang, Y. Zhao, L. Tong, X. Yu, K. Xiong, C. Luo, J. Zhu, F. Wang, Z. Zeng and D. Pan, Tumor aerobic glycolysis confers immune evasion through modulating sensitivity to T cell-mediated bystander killing via TNF-α, *Cell Metab.*, 2023, **35**, 1580–1596.
16 B. Niu, K. Liao, Y. Zhou, T. Wen, G. Quan, X. Pan and C. Wu, Application of glutathione depletion in cancer therapy: Enhanced ROS-based therapy, ferroptosis, and chemotherapy, *Biomaterials*, 2021, **277**, 121110.
17 R. K. Mistry and A. C. Brewer, Redox-Dependent Regulation of Sulfur Metabolism in Biomolecules: Implications for Cardiovascular Health, *Antioxid. Redox Signaling*, 2017, **30**, 972–991.
18 D. B. Rivadeneira, S. Thosar, K. Quann, W. G. Gunn, V. G. Dean, B. Xie, A. Parise, A. C. McGovern, K. Spahr, K. Lontos, R. P. Barnes, M. P. Bruchez, P. L. Opresko and G. M. Delgoffe, Oxidative-stress-induced telomere instability drives T cell dysfunction in cancer, *Immunity*, 2025, **58**, 798–800.
19 C. D. M. Alicea Pauneto, B. P. Riesenberg, E. J. Gandy, A. S. Kennedy, G. T. Clutton, J. W. Hem, K. E. Hurst, E. G. Hunt, J. M. Green, B. C. Miller, S. P. Angus, G. L. Johnson, R. J. Esther, J. L. Guerriero, P. Gao, D. R. Soto-Pantoja, R. L. Ferris, J. L. Modliszewski, M. F. Coleman, H. K. Chung, J. J. Milner, S. J. Moschos, R. L. Wiseman and J. E. Thaxton, Intra-tumoral hypoxia promotes CD8+ T cell dysfunction via chronic activation of integrated stress response transcription factor ATF4, *Immunity*, 2025, **58**, 2489–2504.e8.
20 T. Maj, W. Wang, J. Crespo, H. Zhang, W. Wang, S. Wei, L. Zhao, L. Vatan, I. Shao, W. Szeliga, C. Lyssiotis, J. R. Liu, I. Kryczek and W. Zou, Oxidative stress controls regulatory T cell apoptosis and suppressor activity and PD-L1-blockade resistance in tumor, *Nat. Immunol.*, 2017, **18**, 1332–1341.
21 G. A. Aguirre, M. R. Goulart, J. Dalli and H. M. Kocher, Arachidonate 15-lipoxygenase-mediated production of Resolvin D5n-3 DPA abrogates pancreatic stellate cell-induced cancer cell invasion, *Front. Immunol.*, 2023, **14**, 1248547.
22 C. N. Serhan, S. Libreros and R. Nshimiyimana, E-series resolvin metabolome, biosynthesis and critical role of stereochemistry of specialized pro-resolving mediators (SPMs) in inflammation-resolution: Preparing SPMs for long COVID-19, human clinical trials, and targeted precision nutrition, *Semin. Immunol.*, 2022, **59**, 101597.
23 J. Huang, J. J. Burston, L. Li, S. Ashraf, P. I. Mapp, A. J. Bennett, S. Ravipati, P. Pousinis, D. A. Barrett, B. E. Scammell and V. Chapman, Targeting the D Series Resolvin Receptor System for the Treatment of Osteoarthritis Pain, *Arthritis Rheumatol.*, 2017, **69**, 996–1008.
24 L. A. Horrocks and Y. K. Yeo, Health benefits of docosahexaenoic acid (DHA), *Pharmacol. Res.*, 1999, **40**, 211–225.
25 P. Saito, I. C. Pinto, C. C. A. Rodrigues, R. L. N. de Matos, D. L. Vale, C. P. B. Melo, V. Fattori, T. Saraiva-Santos, S. Mendes-Pierotti, M. M. Bertozzi, A. P. F. R. L. Bracarense, J. A. Vignoli, M. M. Baracat, S. R. Georgetti, W. A. Verri and R. Casagrande, Resolvin D5 Protects Female Hairless Mouse Skin from Pathological Alterations Caused by UVB Irradiation, *Antioxidants*, 2024, **13**, 1008.
26 P. Tangjaidee, P. Swedlund, J. Xiang, H. Yin and S. Y. Quek, Selenium-enriched plant foods: Selenium accumulation, speciation, and health functionality, *Front. Nutr.*, 2023, **9**, 962312.
27 R. Yao, C. He and P. Xiao, 'Food and medicine continuum' in the East and West: Old tradition and current regulation, *Chin. Herb. Med.*, 2022, **15**, 6–14.